International Journal of Heat and Fluid Flow 113 (2025) 109769

Contents lists available at ScienceDirect

International Journal of Heat and Fluid Flow

journal homepage: www.elsevier.com/locate/ijhff

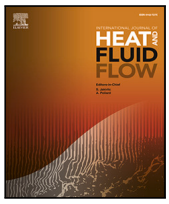

Investigation of blowing and suction for turbulent flow control on a transonic airfoil

A. Frede *, D. Gatti

Institute of Fluid Mechanics, Karlsruhe Institute of Technology, Kaiserstr. 10, Karlsruhe, DE-76131, Germany

ARTICLE INFO

Keywords:
Flow control
Turbulent boundary layer
Transonic flow

ABSTRACT

Active flow control of compressible turbulent boundary layers on airfoils via wall-normal blowing and suction is studied through a comprehensive parametric study. Wall-normal blowing or suction is applied in different positions on either the suction or pressure side of the transonic airfoil RAE2822 and its effect on the aerodynamic efficiency is investigated. The effect of the angle of attack, Mach number, control magnitude, and control position on the result of the active control are discussed. The compressible flow is simulated via Reynolds-averaged Navier–Stokes equations (RANS) with the open-source solver SU2. The inclusive drag as well as a power budget are introduced and calculated to determine the control configurations that decrease the total drag also accounting for the effort to provide and dump the control fluid. The study shows the promising potential of suction on the suction side in the transonic regime where total net drag savings of 16% were achieved in the investigated parameter range. Contrary to previous results, suction leads to a decrease in the total drag, whereas blowing leads to an increase. The appearance of non-linear effects as the shock wave, which is strongly influenced by the active control, contributes to the different performance compared to previous studies, which mostly considered incompressible flows.

1. Introduction

Civil aviation is responsible for around 3% of the global CO_2 emissions (Graver et al., 2019), with an expected increase in the next years due to rising air traffic. A reduction of the fuel consumption and thus the CO_2 emissions is necessary to meet the intended global climate goals. Manipulating the flow around an airfoil with different flow control techniques can lead to a decrease in the total drag and thus an increase in the aerodynamic efficiency. Viscous drag accounts for about half of the total drag of an airplane (Schrauf, 2005), so even small reductions of the viscous drag component can lead to sizable improvements of the aerodynamic efficiency with the associated savings in fuel consumption and thus in CO_2 emissions.

Several flow-control strategies for reducing skin-friction drag have been proposed during the last decades (Gad-el Hak, 2000; Spalart and McLean, 2011). Most of these strategies target the so-called turbulent skin-friction drag, i.e. attempt to reduce the excess drag turbulent flow exhibited compared to their laminar counterparts. Among such strategies, passive methods do not require an external energy input during operation. Prominent in this group is the surface structuring called riblets, which has been proven to lead to skin-friction reductions of about 6% (Walsh, 1986) in laboratory experiments. Tests at flight conditions and transport aircraft confirmed numerical results with drag reductions of 2–6% (Walsh et al., 1989; Szodruch, 1991).

Concerning the wing section, the general design or modification of the airfoil geometry can lead to a shift of the transition point towards the trailing edge, so the change of the flow from laminar to turbulent is delayed, and it can also prevent the boundary layer from separating from the surface. Passive methods, while simpler, achieve only modest skin-friction drag reduction, and they do so mainly in flow conditions close to their design point. Active methods, on the other hand, can be adapted to a broader range of flow conditions and can typically achieve larger values of drag reduction. These advantages come at the cost of the required additional energy input, which needs to be taken into account in the computation of the net benefit of the control.

The active control method of wall-normal blowing and suction is promising because its implementation is rather simple compared to other control methods, and it can be easily integrated into the current aeronautical systems. A small amount of mass is injected into or extracted from the system, which allows the control of the development of the boundary layer. Early investigations by Prandtl and Betz (1932) showed the feasibility of suction in the turbulent boundary layer, where suction was used to prevent flow separation in the adverse pressure gradient regions of boundary layers (Schlichting and Gersten, 1997).

* Corresponding author.
E-mail address: annika.frede@kit.edu (A. Frede).

https://doi.org/10.1016/j.ijheatfluidflow.2025.109769
Received 8 May 2024; Received in revised form 31 January 2025; Accepted 2 February 2025
Available online 17 February 2025

The first theoretical and experimental studies by Mickley et al. (1954) and Black et al. (1958) investigated the effect of the active control method of blowing and suction on a porous flat plate. Their results agree with the previous results from Prandtl and Betz (1932) that suction delays the transition while blowing promotes it. Additionally, they observed that suction decreased the boundary layer thickness and increased the friction drag, while uniform blowing led to the opposite effects. These investigations were conducted in a zero-pressure gradient channel flow. First direct numerical simulations (DNS) by Sumitani and Kasagi (1995) and Park and Choi (1999) agreed with the experimental results.

In the review of Hwang (2004) the control of blowing on flat plates has been proven to be very successful with up to 50% friction drag reduction in subsonic regimes and 80% in supersonic conditions. High-fidelity simulations confirm the findings about the performance of blowing in the turbulent boundary layer (Kametani and Fukagata, 2011; Stroh et al., 2016).

Most of the previous studies (Mickley et al., 1954; Black et al., 1958; Sumitani and Kasagi, 1995; Park and Choi, 1999; Huang et al., 2004; Kametani and Fukagata, 2011; Stroh et al., 2016) focused on the zero-pressure gradient flat plate, where a reduction of the skin friction was found in the control region as well as downstream of the control regime for wall-normal blowing. Additionally, the boundary layer thickness increased due to the added mass, which differs from classic techniques for turbulent skin-friction drag reductions that manipulate wall turbulence without a net mass flux, e.g. riblets (Walsh et al., 1989), wall oscillations (Choi et al., 2002; Yakeno et al., 2014) and traveling waves (Quadrio et al., 2009).

When considering a more complex geometry, such as the one of an airfoil, the problem is becoming more complicated. The geometry changes significantly since a curvature of the surface is present. This means that skin-friction drag is not the only drag source anymore, and other drag components, e.g. pressure drag, also need to be taken into account to achieve an overall reduction in the total drag. Additionally, strong pressure gradients occur along the surface which can lead to non-equilibrium effects. These effects might have a strong influence on the response to the active flow control. Recent studies by Atzori et al. (2020) and Fahland et al. (2021) studied blowing and suction applied on a NACA4412 with incompressible LES and RANS simulations, respectively. They showed that blowing and suction have the potential for a reduction of the drag, where the configuration of blowing on the pressure side is the most promising. Fahland et al. (2021) revised the published results from 2021 and showed that, at least for the configurations addressed in their study, no overall net drag saving can be achieved when taking into account the effort of providing the fluid for blowing or dumping it after suction.

Considering a flight case in civil aviation, the flow around the wing will be in the transonic regime. In this regime, weak shock waves occur on the suction side of the airfoil. An extension of the above described studies on the effect of the active control on an airfoil to the compressible and transonic regime at real flight parameters is necessary to get estimations of the drag reductions that can be achieved at these parameters. The interaction of the shock wave and the active control method of homogeneous wall-normal blowing and suction needs to be investigated in a compressible and transonic flow.

In the present work, the feasibility of wall-normal homogeneous blowing and suction to improve the aerodynamic efficiency of the transonic airfoil RAE2822 is investigated by taking into account compressibility effects as well as transonic flow with the occurrence of shock waves. The questions that should be answered in this work are

1. How well does the active control method of wall-normal homogeneous blowing and suction perform when taking into account compressibility effects in the subsonic flow?
2. What effect does the shock on the suction side and the presence of non-linear effects in the transonic regime have on the performance of the active flow control?

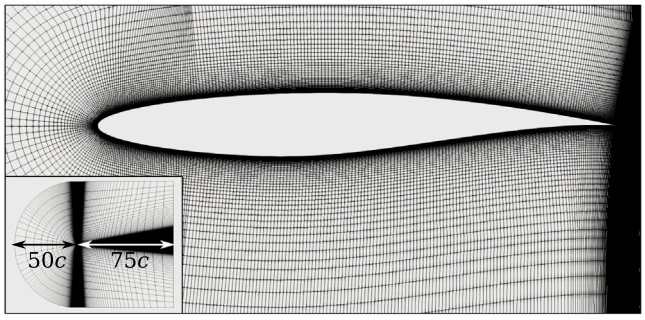

Fig. 1. Sketch of the computational C-mesh.

To answer these two questions, a detailed numerical study is conducted where the active control method of wall-normal homogeneous blowing and suction is investigated. The variation of many parameters, such as the Mach number, the angle of attack, and the control parameters such as the control configuration, magnitude, and position are investigated.

The paper is structured into 4 sections. In Section 2 the numerical methods and the applied boundary conditions are described as well as the calculation of the power budget and the net drag. The results of the parametric study are described and discussed in Section 3. Section 4 summarizes the results and findings.

2. Methodology

2.1. Numerical methods

The compressible flow around the transonic airfoil RAE2822 is simulated via Reynolds-Averaged Navier–Stokes equations (RANS) with the open-source solver SU2 (Economon et al., 2015). For the simulations, the density-based steady-state solver is used. The Menter k-ω-SST model is employed as the turbulence model. A fixed transition at $x/c = 0.1$, with c being the chord length and x the coordinate in stream-wise direction, is implemented via a semi-implicit scalar source. The tripping location spans 1%c in streamwise direction, and the size of the local boundary layer thickness in wall-normal direction. The fluid is modeled as standard air and treated as an ideal gas with the viscosity calculated by the Sutherland model.

The numerical grid consists of hexahedral cells and has a 2D block-shaped pattern. It has a C-radius of $r_c = 50c$ and an outlet distance of $d_o = 75c$, where c is the chord length of the airfoil. A sketch of the mesh is shown in Fig. 1. The total cell count of the meshes is $n_{cell} \approx 150000$. A y^+ value of 1 or less is assured in the first cell of the boundary layer. The boundary layer consists of at least 40 points. The growth factor near the wall is 1.1, so a detailed resolution of the flow near the wall is provided. The meshes are generated with a custom script using *blockMesh* from OpenFoam and are then converted into a readable format for SU2. For a detailed description of the mesh generation, see Fahland et al. (2021).

The convective fluxes are discretized with the second order *Roe* method (Roe, 1981) and the viscous fluxes with the *Green-Gauss* method (Ferziger and Perić, 2002). For the gradients of turbulent variables, the second-order upwind scheme is applied.

2.2. Boundary conditions

The airfoil's surface is simulated as an adiabatic wall. In the non-control regions, the velocity in the normal direction on the airfoil surface is set to zero, so a no-slip boundary condition is present. In the area of control, a homogeneous wall-normal mass flow rate is prescribed, while the velocity and energy fluxes are determined by extrapolating thermodynamic properties using the Riemann invariants.

For blowing, the density of the control fluid is approximated by the density of the closest point in the flow. The outer boundaries of the computational domain use a non-reflective far-field boundary condition aligned with the local directions of the characteristics.

In most of the simulations performed in the present study, the region on which blowing and suction is applied spans from $x/c = 0.25$ to 0.85. The late start of the control region allows the flow to become fully turbulent before the control region starts. The endpoint of $x/c = 0.85$ was chosen so that trailing edge components can still be implemented without overlapping with the control region. In Section 3.1.4, the influence of the position of the control area was also analyzed. Unless otherwise stated, the following results always refer to the control area described above.

In the parametric study, three different control configurations were investigated: blowing on the pressure side, suction on the suction side, and blowing on the suction side. All three configurations are investigated individually, and no combinations of two configurations are considered.

2.3. Net drag

The drag coefficient for an airfoil can be calculated by integrating the pressure and friction stresses along the surface, which results in the body drag $c_{D,body}$, or it can be determined from the momentum loss in the wake, which results in the wake drag $c_{D,wake}$. For an uncontrolled case or a controlled case with zero total mass flow, which means that the mass flow of the fluid sucked in is the same as the mass flow of the blowing fluid, the two drag components are equal. The active flow control of blowing and suction, where fluid is either removed or expelled, changes this relationship. In the case of blowing, a mass source is present on the airfoil surface, since the air intake is not explicitly defined in the current investigated system. The fluid that is expelled in wall-normal direction lacks momentum in the main wind direction, so it needs to be accelerated towards the wake of the airfoil. The reaction force is carried by the body, which results in a reduced body drag compared to the wake drag.

For suction, the opposite occurs, and thus the wake drag is reduced compared to the body drag, as shown by Beck et al. (2018). For both suction and blowing, the largest among $c_{D,body}$ and $c_{D,wake}$ is the drag component, which includes the costs of providing or expelling the flow control fluid. This is the so-called inclusive drag $c_{D,inc}$, which is used in the analysis of the results for a comparison of the different investigated cases.

$$c_{D,inc} = \begin{cases} c_{D,body} = c_{D,wake} + c_{BLC} & \text{for suction} \\ c_{D,wake} = c_{D,body} + c_{BLC} & \text{for blowing} \end{cases} \tag{1}$$

Here, the boundary layer control penalty c_{BLC} is proportional to the mass flow rate (Fahland et al., 2024)

$$c_{BLC} = \left| 2 \frac{u_{BLC}}{U_\infty} \frac{l_{BLC}}{c} \frac{\varrho_{BLC}}{\varrho_\infty} \right|, \tag{2}$$

with the velocity of the control fluid u_{BLC} and the free-stream velocity U_∞. The length of the control system is described by l_{BLC}, while the control fluid has a density of ϱ_{BLC} and the free stream of ϱ_∞.

2.4. Power budget

Additionally to the control penalty drag c_{BLC} due to the non-zero mass flow rate, the power required to operate the active control must be taken into account to assess the net efficiency increase. The focus of the current study is the investigation of the influence of different control configurations. Therefore, no combinations of blowing and suction are studied, and the net control mass flow rate is always non-zero. The details of the air supply (for blowing) or dumping (for suction) strongly influence the required control power but are not explicitly defined here, since they greatly depend on the particular physical implementation of the active control, which is not addressed in the present study. Therefore, an accurate calculation of the additional power is not possible, and many simplifying assumptions have to be made here. In this respect, we follow the approach of Fahland et al. (2021) for the estimation of the additional power. Although this estimate reflects a worst-case scenario, it can be calculated and understood with just a few assumptions and limited complexity.

The additional control power is defined as the power needed to overcome the pressure difference between the fluid supply and the controlled surface for blowing, or from the controlled surface to the position of discharge for suction.

The power consumption is converted to dimensionless drag components so that the efficiency can be calculated with the extra cost (Beck et al., 2018). It is assumed that the fluid from suction is expelled at a pressure coefficient of $c_p = 1$ and the fluid for the blowing control is collected at stagnation, where also $c_p = 1$ is valid. So the total drag coefficient results in

$$c_{D,total} = \begin{cases} c_{D,body} - c_{BLC} + c_{pump} & \text{for suction} \\ c_{D,body} + c_{BLC} + c_{turbine} & \text{for blowing} \end{cases} \tag{3}$$

where c_{pump} accounts for the energy that is needed to drive the pump for suction and $c_{turbine}$ reflects the energy that can be regained by a turbine during the blowing process.

For the suction control, extra energy is needed for the actual suction process, which is expressed by c_{pump}. The sucked fluid can now be expelled somewhere on the airfoil surface to generate some thrust. We assume to expel the fluid at $c_p = 1$, since at this specific pressure coefficient the thrust equals the boundary layer penalty c_{BLC}. For the blowing process, the costs for the fluid supply can be calculated by the boundary layer control penalty, while some energy can be regained from the turbine.

To calculate the pump drag for suction or the turbine drag for blowing, the pressure differences between the supply chamber and the sink or source, respectively, need to be determined. The sink and the source are at free-stream total pressure level.

The pressure of the supply chambers is at a constant pressure level, which is calculated by the following equation

$$c_{p,chamber} = \begin{cases} min\{c_{p,control}\} - 0.1 & \text{for suction} \\ max\{c_{p,control}\} + 0.1 & \text{for blowing} \end{cases} \tag{4}$$

where $c_{p,control}$ is the pressure coefficient in the control area, and the maximum or minimal value is used for blowing or suction, respectively. For suction, the pressure level in the supply chamber needs to be lower compared to the pressure level on the control surface, therefore, $\Delta c_p = 0.1$ was subtracted from the minimal pressure value (Beck et al., 2018). The opposite holds for blowing, the pressure level in the supply chamber needs to be higher than on the control surface, so $\Delta c_p = 0.1$ was added to the maximum pressure value. The different pressure levels are also shown in Fig. 2.

This choice does not reflect the best option but gives an estimation of the costs for the control. Especially for configurations with large pressure differences in the control area, as they are present in the cases where a shock wave appears on the suction side, this estimation is a very conservative approximation. For a more detailed discussion of the applied power calculation, see Section 3.2.

The pump and turbine drag are calculated as follows

$$c_{pump} = \frac{1}{\eta_p} \frac{u_{BLC}}{U_\infty} \frac{l_{BLC}}{c} \frac{\varrho_{BLC}}{\varrho_\infty} (1 - c_{p,chamber}) \tag{5}$$

$$c_{turbine} = -\eta_t \frac{u_{BLC}}{U_\infty} \frac{l_{BLC}}{c} \frac{\varrho_{BLC}}{\varrho_\infty} (1 - c_{p,chamber}) \tag{6}$$

with a pump efficiency of $\eta_p = 0.7$ and a turbine efficiency of $\eta_t = 0.7$ (Beck et al., 2018).

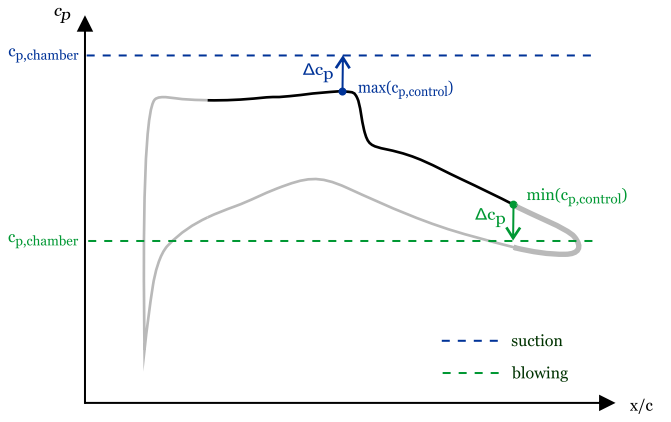

Fig. 2. Sketch of a pressure distribution to determine the different pressure levels for the supply chambers for the pump or turbine.

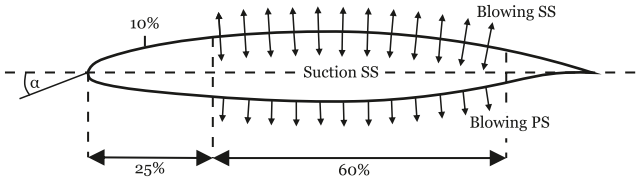

Fig. 3. Sketch of the control areas and different control configurations.

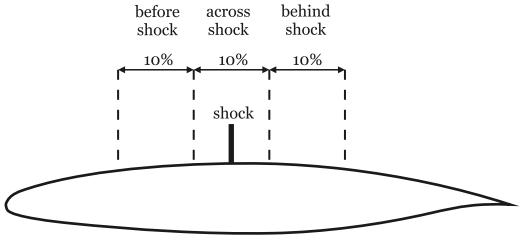

Fig. 4. Sketch of the different control positions with respect to the shock position.

2.5. Parametric study

A parametric study was conducted to investigate the effect of wall-normal blowing and suction on the transonic airfoil RAE2822 in a compressible and subsonic or transonic flow. All simulations were conducted at a chord based Reynolds number of about $Re = 5 \times 10^6$. The Mach number was varied between $Ma = 0.6$, which corresponds to the subsonic flow case up to $Ma = 0.729$, the design Mach number for the present airfoil, representing the fully transonic case. The control magnitude is expressed in terms of mass flow rate and ranges between $\dot{m}_{BLC} = 0.1\%\dot{m}_\infty$ up to $3\%\dot{m}_\infty$ with the free-stream mass flow per unit area of $\dot{m}_\infty = U_\infty c \varrho_\infty$. The angle of attack varies between $\alpha = -1°$ and $\alpha = 3°$.

Three different control configurations are investigated: blowing on the suction side, suction on the suction side, and blowing on the pressure side. In Fig. 3 a sketch of the airfoil and the different control configurations is shown. In the results, also the influence of varying the position at which blowing or suction is applied is analyzed. To this aim, three additional control positions are introduced, named before shock, across shock, and behind shock. These control areas have a size of $10\%c$ and their positions are defined with respect to the shock position in the uncontrolled cases. A graphical sketch of the positions is shown in Fig. 4. For all other configurations, the default control area of $x/c = 0.25 - 0.85$ is used.

For all combinations of Ma and α the uncontrolled reference cases are calculated. These results were used as restart files for the controlled cases to save computational time.

The freestream parameters are based on a flight altitude of 11 km at standard atmosphere. For the simulations, a Reynolds number of $Re = 5 \times 10^6$, a free stream temperature of $T_\infty = -53.5$ °C, a viscosity of $\mu_\infty = 1.449 \times 10^{-5} \frac{\text{kg}}{\text{ms}}$ and the corresponding Mach number are prescribed. The density and the pressure are calculated from the given parameters and the ideal gas law.

The Mach number varies between $Ma = 0.6 - 0.8$, so the range of subsonic up to transonic flow regimes is covered. The Reynolds number of the simulation is smaller compared to a real airplane with a Reynolds number of about $Re = 20 \times 10^6 - 30 \times 10^6$, depending on the size of the airplane. This regime cannot be covered in this study, because the computational costs for such high Reynolds numbers are too high. So all calculations have been conducted at lower Reynolds numbers of $Re = 5 \times 10^6$.

3. Results

3.1. Parametric study

3.1.1. Effect of control configuration

In the parametric study, three different control configurations were investigated: blowing on the pressure side, blowing on the suction side, and suction on the suction side. The effect of the different control configurations should be discussed in this section. In Fig. 5 the polar plots and the pressure and friction coefficient distribution are plotted for a Mach number of $Ma = 0.6$ in the left column (subsonic uncontrolled case) and $Ma = 0.725$ in the right column (transonic uncontrolled case). The control magnitude is $\dot{m}_{BLC} = 0.1\%\dot{m}_\infty$ and the angle of attack is $\alpha = 2.31°$ for the c_p and c_f plots. The angle of attack of $\alpha = 2.31°$ is marked by the circled symbols in the polar plot. To increase the readability of the data and prevent them from overlapping, the c_f values from the lower surface of the airfoil are plotted as negative values.

First, the subsonic cases at a Mach number of 0.6, which are shown in the left column of Fig. 5, are analyzed. All polars show a similar trend in which the lift and drag coefficients increase with increasing angle of attack. Since no complete flow separation is observed, no sudden changes in the slope are expected. The slope of the polars for suction on the suction side and blowing on the pressure side increased compared to the uncontrolled case, while the slope for blowing on the suction side decreased. All controlled polars are shifted to higher drag values compared to the uncontrolled case, except for the high lift configurations of suction on the suction side. Especially for the two blowing configurations, the inclusive drag coefficient increased by around 20%. For suction on the suction side, the drag difference at lower lift configuration is significant but decreases with increasing angle of attack and lift. At $\alpha = 2.31°$ the two polars intersect, and the drag coefficient of the case with suction on the suction side has a lower drag coefficient than the uncontrolled case. For these high lift configurations, an increase in the efficiency is reached. The distribution of the pressure coefficient changes slightly depending on the control configuration, see Fig. 5(c). Blowing on the suction side leads to a slightly increased pressure coefficient on the whole upper side. Opposite effects can be observed for suction on the suction side with a slightly decreased pressure coefficient. The slightly decreased pressure coefficient results in a small increase in lift coefficient compared to the uncontrolled case for a constant angle of attack. Blowing on the

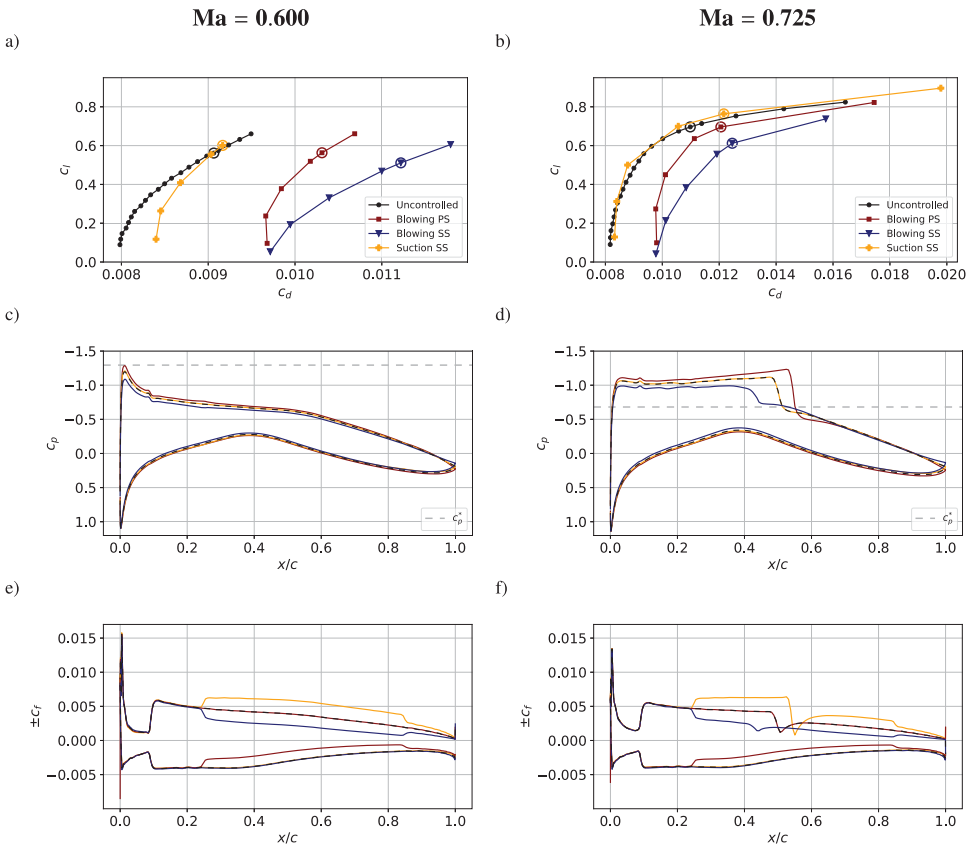

Fig. 5. Polar plot and pressure and friction coefficient distribution for the three control configurations and the uncontrolled reference case for $\dot{m}_{BLC} = 0.1\%\dot{m}_\infty$ and $\alpha = 2.31°$ for the surface distribution plots, and $Ma = 0.6$ and 0.725 for the left and right columns, respectively.

pressure side leads to a decrease in the pressure coefficient on the lower side. A clear effect of the control can be observed for the friction coefficient (see Fig. 5(e)). In the control region, a clear increase can be seen for suction, whereas a decrease can be observed for blowing. Suction removes fluid from the boundary layer, and thus the boundary layer thickness is thinner. The velocity gradient in the boundary layer increases, which then results in an increase in the wall-shear stress and thus an increased friction coefficient. For blowing, the opposite effects can be observed.

Secondly, the transonic case at a Mach number of $Ma = 0.725$ which is shown in Fig. 5 in the right column is studied. The trend of the polars is similar to the subsonic cases, an increase in the angle of attack leads to an increased drag and lift coefficient. For suction on the suction side, most configurations show a decreased drag coefficient compared to the uncontrolled case, which results in an increased efficiency. The other two configurations, blowing on the pressure and suction side, lead to an increased drag. The pressure distributions show a clear dependency on the different control configurations. For blowing on the pressure side, the pressure distribution on the upper side matches the one of the uncontrolled case, whereas a small decrease of c_p on the lower side can be observed. Both control configurations on the upper side have a significant influence on the shock position and magnitude. For the uncontrolled case, covered by the red curve, the shock position is at $x/c = 0.51$. Blowing on the suction side leads to a shift of the shock towards the leading edge to $x/c = 0.44$ and a decrease in the shock magnitude, whereas opposite effects can be observed for suction on the suction side: the shock is shifted towards the trailing edge to $x/c = 0.55$ and the shock magnitude increased significantly. Before the shock, a near constant pressure coefficient can be observed, followed by a significant increase in c_p at the shock position and a steady increase towards the trailing edge. The sonic c_p^* value is also indicated in the pressure distribution for the corresponding Mach number.

Similar to the subsonic case, an increase (or decrease) of the friction coefficient in the control region can be observed for suction (or blowing). The shock is indicated by a sharp drop of c_f followed by a slight recovery.

In agreement with previous literature (Mickley et al., 1954; Black et al., 1958; Sumitani and Kasagi, 1995; Park and Choi, 1999; Hwang, 2004) blowing leads to a reduction of the friction drag of up to 40% for the transonic cases with a medium mass flow rate. However, when the inclusive drag is calculated, which also includes the pressure drag component and the boundary layer control penalty, an increase in the inclusive drag is observed compared to the uncontrolled cases.

Overall it can be concluded, that the only control configuration that can lead to an increase in efficiency is suction on the suction side for rather high lift configurations, if taking into account the inclusive drag.

3.1.2. Effect of control magnitude

The effect of the control magnitude is discussed in this section. The left column of Fig. 6 shows the subsonic uncontrolled case at $Ma = 0.65$ and the corresponding controlled cases with suction on the suction side at an angle of attack of 2.31°, marked by circled symbols in the polar plot. The polar plot clearly shows a shift of the c_l-c_d curves to higher drag values with increasing control magnitude. The lift coefficient at the same angle of attack also increases with increasing control magnitude. Nevertheless, the aerodynamic efficiency is smaller than the one for the uncontrolled cases. For high lift configurations and a rather small control magnitude of $\dot{m}_{BLC} < 0.2\%\dot{m}_\infty$ slightly lower drag values compared to the uncontrolled polar (black) can be observed. From the polar plot, it can be summarized that especially the cases with a small control magnitude are promising for an efficiency increase.

In the pressure distribution, it can be observed that the uncontrolled case, indicated in black, is subsonic and no shock is present on the upper side of the airfoil. With increasing magnitude of the suction on the

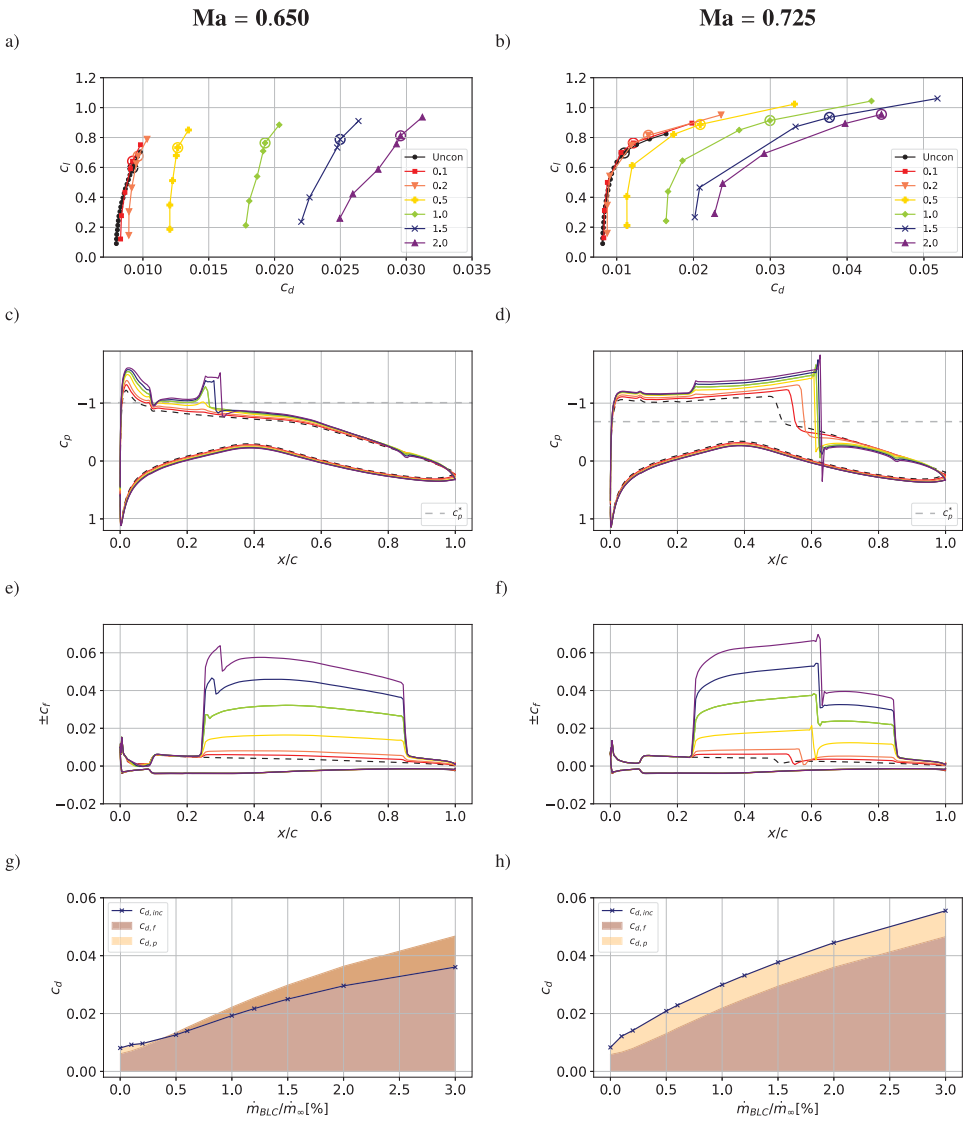

Fig. 6. Polar plot and pressure and friction coefficient distribution for different control magnitudes and the uncontrolled reference case. The applied control is suction on the suction side at Mach numbers of $Ma = 0.65$ and 0.725 for the left and right columns, respectively. The surface plots are shown for an angle of attack of $\alpha = 2.31°$.

upper side, a pressure decrease followed by a sudden pressure increase around $x/c = 0.22 - 0.28$, dependent on the control magnitude, can be observed, which leads to the appearance of a shock for high control magnitude configurations ($\dot{m}_{BLC} \geq 1\%\dot{m}_\infty$). Suction on the upper side also influences the flow on the lower side, which can be observed by a slightly increased pressure coefficient. This effect increases with increasing control magnitude. The increase of the pressure coefficient on the lower side and the presence of the shock for higher control magnitude explain the lift increase observed in the polar plot for higher control magnitudes.

Suction on the suction side leads to an increase in the friction coefficient on the upper surface as expected. The increase in the friction coefficient grows with increasing control magnitude. The presence of the shock can also be observed in the friction coefficient and is indicated by a strong decrease in c_f.

The inclusive drag is the sum of the pressure and friction drag as well as the boundary layer control penalty. The last plot in the left column shows the pressure and friction drag ratios compared to the total drag. Since the body drag for the control of suction already includes the boundary layer penalty, it is not also plotted in Fig. 6(g). The blue curve indicates the inclusive drag, which consists of a friction part, shown in red, and a pressure part, shown in yellow. For a control magnitude of $\dot{m}_{BLC} \geq 0.5\%\dot{m}_\infty$ the blue curve cuts the ratio of the friction component. This indicates that a negative pressure drag is present and thus the inclusive drag is lower than the friction component. This is shown by the orange color, which is an overlap of the red and the yellow area.

In the transonic case for a Mach number of $Ma = 0.725$, right column of Fig. 6, it can be seen that the low magnitude control configurations ($\dot{m}_{BLC} \leq 0.2\%\dot{m}_\infty$) at high lift coefficients lead to slightly lower drag values compared to the uncontrolled case. The overall trend of the polars is similar to the one of the subsonic case, with increasing mass flow rate of the control fluid, the polars are shifted to higher drag values and also to higher lift values.

The increase in the lift coefficient can be explained by the shift of the shock position towards the trailing edge for increasing control magnitude, see Fig. 6(d), and the increase in the shock magnitude. In the friction coefficient distribution in Fig. 6(f), an increase in the friction coefficient with increasing control magnitude can be observed. The increase in the friction coefficient can also be seen in Fig. 6(h), where the friction ratio is marked by the red area, which increases with increasing control magnitude. The ratio of the pressure component is almost constant, marked by the yellow area, and is now positive, compared to the subsonic case, which leads to higher inclusive drag values.

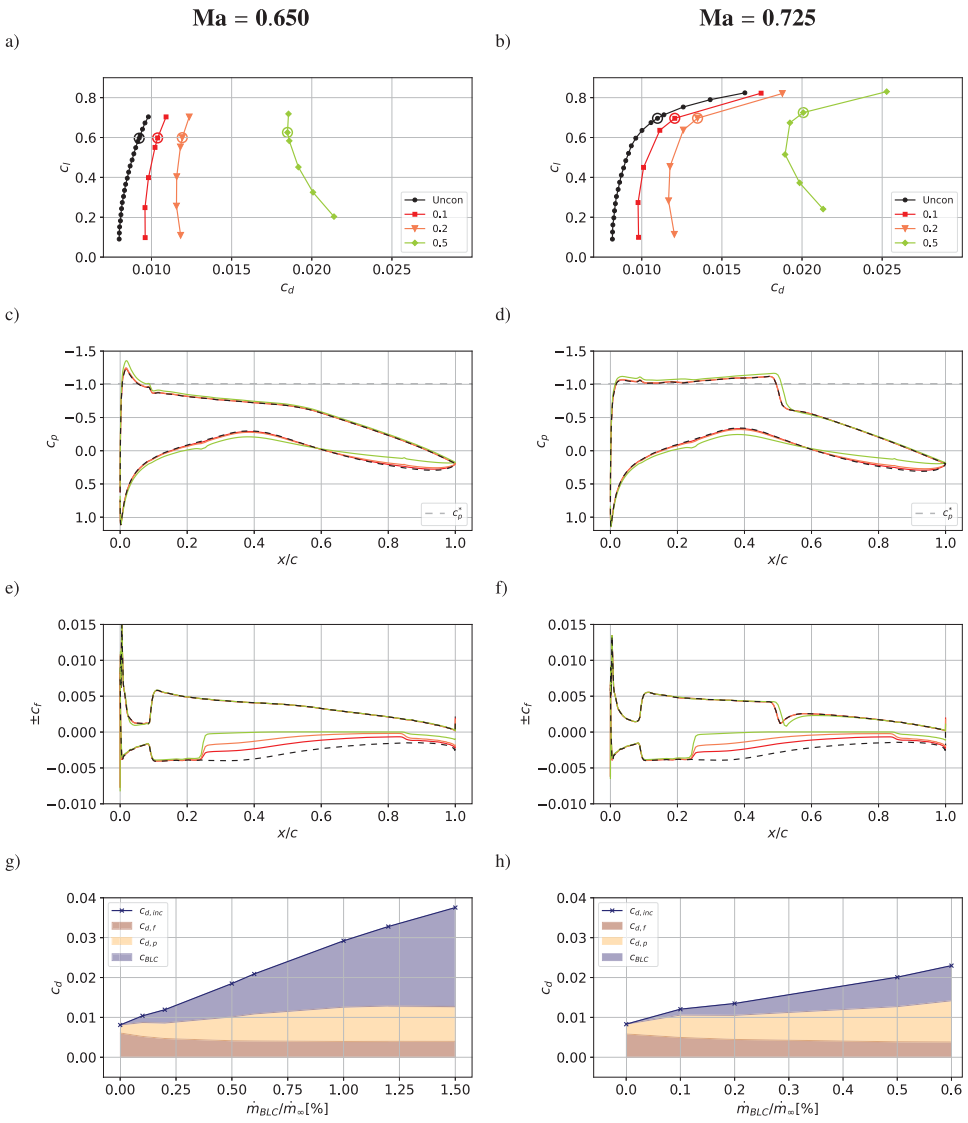

Fig. 7. Polar plot and pressure and friction coefficient distribution for different control magnitudes and the uncontrolled reference case. The applied control is blowing on the pressure side at Mach numbers of $Ma = 0.65$ and 0.725 for the left and right columns, respectively. The surface plots are shown for an angle of attack of $\alpha = 2.31°$.

The effect of the control magnitude for blowing on the pressure side is shown in Fig. 7. In the uncontrolled subsonic case (black) with a Mach number of 0.65, left column, an increase in the drag coefficient with increasing angle of attack can be observed, while a significant increase in the lift coefficient can be observed. For the low magnitude controlled cases, the trend is the same, but the polar is shifted to slightly higher drag values. For higher control magnitudes, $\dot{m}_{BLC} \geq 0.5\%\dot{m}_\infty$, the trend changes and the drag coefficient decreases with increasing angle of attack accompanied by an increase in the lift coefficient. For control magnitudes $\dot{m}_{BLC} \geq 0.5\%\dot{m}_\infty$, massive separation occurs at the lower side due to the injected fluid. Flow snapshots with local streamlines are shown in Fig. 8 where the flow separation in the back part of the airfoil can be seen.

The pressure coefficient for $\alpha = 2.31°$ for the uncontrolled case, compare Fig. 7(c) (dashed black curve), increases over the whole upper side. On the pressure side, the pressure coefficient decreases up to $x/c = 0.4$ and then changes its slope and increases continuously towards the trailing edge. For low control magnitudes, the trend of the pressure distribution only changes slightly, with a small decrease in the pressure coefficient on the upper side. On the lower side, the pressure coefficient increases in the region up to $x/c \leq 0.58$ and decreases in the back part of the airfoil compared to the uncontrolled case. At higher control magnitudes $\dot{m}_{BLC} \geq 1\%\dot{m}_\infty$, blowing on the pressure side leads to a shock on the suction side close to the leading edge, which is associated with a strong increase in the pressure coefficient. On the pressure side, it can be observed that the pressure coefficient is almost constant and close to zero in the region of $x/c \approx 0.4$ towards the trailing edge, which indicates separation. As already seen in Fig. 8 the flow detaches when the control magnitude is larger than $0.5\dot{m}_\infty$ which can be seen by the smaller pressure gradient and the zero friction coefficient. In the area where the flow is detached, the injected fluid is still present and gets deflected towards the outer flow. The friction coefficient behaves as expected: it decreases more and more in the region of blowing with increasing control magnitude up to a control magnitude of $\dot{m}_{BLC} \leq 0.5\%\dot{m}_\infty$. For higher control magnitudes, the friction coefficient in the control region is zero, and the flow is detached. Due to the flow of the control fluid in the wall-normal direction, no friction is present in this area, as well as no backflow. When the blowing region ends at $x/c = 0.85$, a full separation with backflow, which can be denoted by a negative friction coefficient, can be observed for high control magnitudes of $\dot{m}_{BLC} \geq 1\%\dot{m}_\infty$.

With increasing control magnitude, the friction drag is slightly decreasing, while the pressure drag increases, see Fig. 7(g). The main contribution to the drag is the boundary layer penalty drag, which

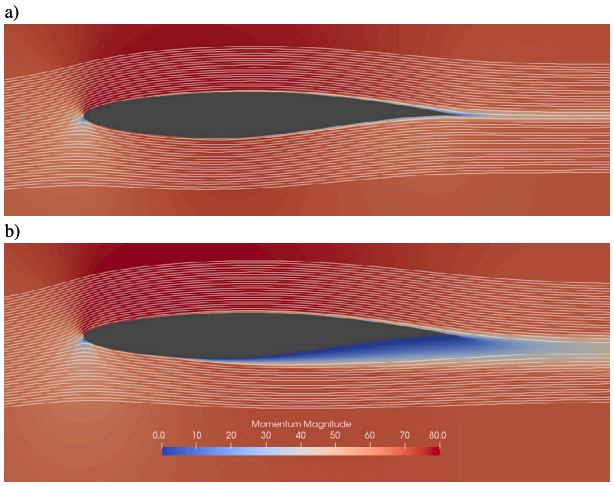

Fig. 8. Snapshot of the streamlines for (a) the uncontrolled case and (b) the controlled case with blowing on the pressure side for $Ma = 0.65$, $\alpha = 2.31°$ and $\dot{m}_{BLC} = 1.2\%\dot{m}_{\infty}$.

increases significantly with increasing control magnitude and is responsible for about 57% of the total drag for a control magnitude of $\dot{m}_{BLC} = 1\%\dot{m}_{\infty}$.

The figures for the transonic case are shown in the right column of Fig. 7. In the polar plot, only the data up to a control magnitude of $\dot{m}_{BLC} \leq 0.6\%\dot{m}_{\infty}$ are presented since no steady solution can be obtained for higher control magnitudes. The polars are shifted to higher drag values but also higher lift coefficients with increasing control magnitude. In the pressure distribution (see Fig. 7(d)) a slight decrease of the pressure coefficient before the shock position for small control magnitudes can be observed while the shock position is shifted towards the trailing edge. On the pressure side, the same effect as in the subsonic case can be seen, the pressure coefficient in the control area is almost constant. The shift in the shock position and magnitude increases with increasing control magnitude, even though the control takes place at the opposite side of the airfoil.

On the pressure side, the friction coefficient in the control area is again zero, as also seen in the subsonic case.

3.1.3. Effect of Mach number

In Fig. 9 the results for a variation of the Mach number are shown for the control of suction on the suction side with a control magnitude of $\dot{m}_{BLC} = 0.2\%\dot{m}_{\infty}$. In this section, the polar and surface plots have been omitted for reasons of clarity. The trends of the corresponding curves have already been described in detail in the previous sections. The Mach number regime covers the range from subsonic $Ma < 0.7$ up to the transonic regime $Ma \geq 0.7$, where a clear shock is observed at the upper side of the airfoil. An increase in the Mach number leads to, first, the appearance of the shock and, later, to a shift of the shock towards the trailing edge and an increase in magnitude.

In Fig. 9 the drag distribution is shown. The components for the controlled cases are shown by the colored areas and the blue line, while the uncontrolled components are marked by the dashed and dotted lines. For the uncontrolled and the controlled case, a slight decrease in the friction drag is observed with an increase in the Mach number. The friction drag of the uncontrolled case is lower compared to the controlled one, which can be explained by the applied control of suction on the suction side, which leads to an increase in the friction drag, as already seen in Section 3.1.1. The inclusive drag, so the sum of the pressure and body drag, which already includes the boundary layer control penalty, is almost constant for both the controlled and the uncontrolled case up to a Mach number of $Ma = 0.7$. At this Mach number, the shock appears, which leads to a significant increase in the pressure drag. With a further increase of the Mach number, also the

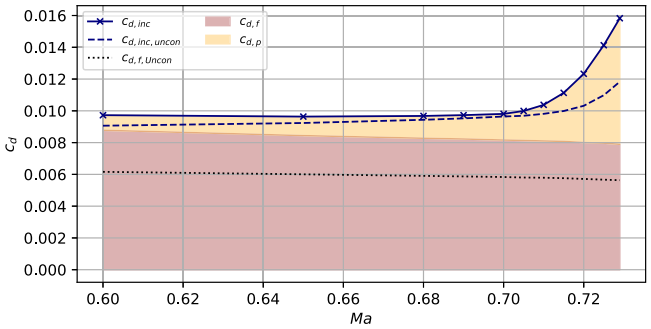

Fig. 9. Drag distribution for different Mach numbers for suction on the suction side with a control magnitude of $m_{BLC} = 0.2\%\dot{m}_{\infty}$ and an angle of attack of $\alpha = 2.31°$.

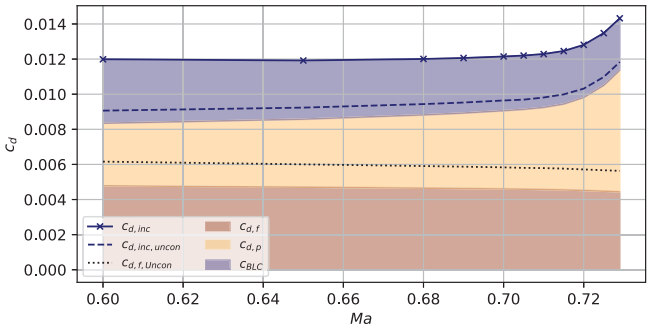

Fig. 10. Drag distribution for different Mach numbers for blowing on the pressure side with a control magnitude of $m_{BLC} = 0.2\%\dot{m}_{\infty}$ and an angle of attack of $\alpha = 2.31°$.

pressure drag increases, which is due to the increase in the shock's magnitude. At $Ma = 0.725$ the pressure drag is responsible for about 46% of the total drag.

The effect of the variation of the Mach number for blowing on the pressure side is shown in Fig. 10. Since the control is applied to the lower side of the airfoil, the influence on the flow and thus the shock's characteristics on the upper side are rather low. However, due to the variation of the Mach number, a shift of the shock position as well as an increase in magnitude is still observed. But no significant variation between the controlled and uncontrolled cases can be seen on the upper side. In the drag distribution in Fig. 10 it can be observed, that the trend is similar to the cases with suction on the suction side because the main reason for the increase of the pressure drag component can be explained by the shift of the shock, which is mainly driven by the variation of the Mach number. This effect can be increased by the control of suction on the suction side. The comparison of the uncontrolled and controlled configurations for blowing on the pressure side shows an increased friction drag compared to the uncontrolled case, contrary to the suction case. Blowing increases the boundary layer thickness and thus leads to a reduction of the friction drag. As already observed in the previous case, the appearance of the shock at $Ma \approx 0.7$ leads to a significant increase of the pressure component.

3.1.4. Effect of control position

The influence of the control position is shown in Fig. 11 for the transonic Mach number of $Ma = 0.725$ and the control configurations of blowing on the suction side and suction on the suction side in the left and right columns, respectively. The default control area spans 60% of the chord length, while the smaller areas of before, across, and behind shock span 10% of the chord length. The positions are defined concerning the shock position in the uncontrolled case, see Fig. 4. The effect of the control, so a shift of the shock position and change in magnitude, can also be observed for the smaller control areas for both investigated control configurations, but with a much smaller effect, see

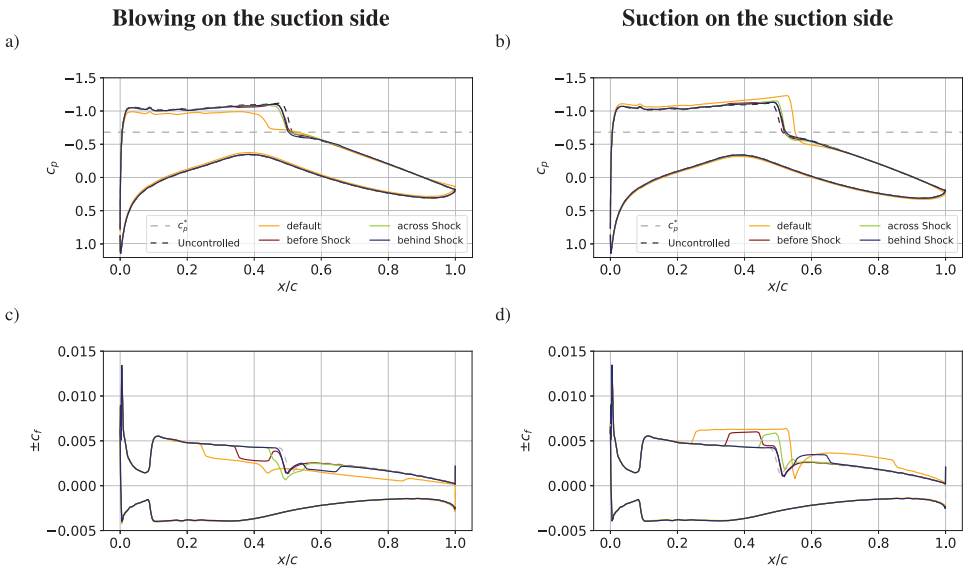

Fig. 11. Polar plot and pressure and friction coefficient distribution for different control positions and the uncontrolled reference case. The applied control is blowing on the suction side and suction on the suction side for the left and right columns, respectively, with a control magnitude of $m_{BLC} = 0.1\%\dot{m}_{\infty}$. The surface plots are shown for an angle of attack of $\alpha = 2.31°$.

Fig. 4(a) and (b). The control intensity depends on the free-stream flow, and therefore the total mass flow is smaller due to the smaller area through which the flow passes. The trend of the friction coefficient shows that only the areas in which the control is applied show a large difference from the uncontrolled case. It can also be seen that the shift of the shock is the same for the positions before and behind the shock, while the shift of the shock for the control at the shock position is minimally larger but still significantly smaller than in the default case.

3.2. Efficiency increasing configurations

The previously discussed results show that there are a few configurations where an increase in efficiency was observed. In this subsection, these cases should be analyzed in more detail.

The only control configuration that showed an increase in efficiency is suction on the suction side at low control magnitudes of $\dot{m}_{BLC} = 0.1$ in the default control area. Promising cases have been observed throughout the whole investigated range of Ma numbers. For the following comparison, three example Mach numbers were chosen: 0.65 to represent a subsonic case and 0.71 and 0.725 in the transonic regime. All the cases are listed in Table 1.

The controlled cases are now compared to uncontrolled cases at the same lift coefficient instead of the same angle of attack. The uncontrolled simulations were rerun at the same c_l from the corresponding controlled cases. This change in comparison is especially important for those cases, which are far from the design angle of attack. In fact, in this case, the control at low AoA configurations showed a high efficiency increase compared to the uncontrolled cases at the same AoA. However, a comparison at the same lift coefficient has shown that these configurations are far from increasing the efficiency.

For all configurations, the angle of attack for the uncontrolled cases is slightly higher $\Delta\alpha = 0.2° - 0.6°$ compared to the uncontrolled cases. A comparison of the controlled cases with the corresponding uncontrolled cases at the same lift coefficient showed that with increasing AoA the effectiveness of suction improves so that for large AoA the control does induce an overall net efficiency increase. For lower Mach numbers, the efficiency increase is smaller than for the higher transonic cases. In the subsonic regime, a maximum efficiency increase of about 5.75% is reached for a lift coefficient of $c_l = 0.752$. For the controlled case, this corresponds to an angle of attack of $\alpha = 3°$ and for the uncontrolled case of $\alpha = 3.32°$. In the fully transonic regime, the efficiency increase is 22.59% for $c_l = 0.897$ for a controlled angle of $\alpha = 3°$ and for the uncontrolled case $\alpha = 3.574°$. The maximum absolute value of the efficiency of $Eff = 62.25$ is reached for a lift coefficient of $c_l = 0.700$. An application of the active control in this case led to an increase in

Table 1
Example cases of suction on the suction side, which promise an increase in efficiency. The uncontrolled cases are rerun at the same lift coefficient as the controlled cases for a better comparison.

Ma	$\dot{m}_{BLC}$	AoA	c_l	$c_{d,body} \cdot 10^2$	Eff	
0.65	0.1	−1°	0.121	0.83	15.57	−3.78%
0.65	–	−0.797°	0.121	0.80	15.15	
0.65	0.1	0°	0.277	0.84	33.11	−2.27%
0.65	–	0.224°	0.277	0.82	33.87	
0.65	0.1	1°	0.434	0.86	50.21	−0.46%
0.65	–	1.250°	0.434	0.86	50.44	
0.65	0.1	2°	0.592	0.91	65.35	**1.54%**
0.65	–	2.279°	0.592	0.92	64.37	
0.65	0.1	3°	0.752	0.98	76.59	**5.75%**
0.65	–	3.324°	0.752	1.04	72.42	
0.71	0.1	−1°	0.127	0.83	15.30	−2.22%
0.71	–	−0.785°	0.127	0.81	15.65	
0.71	0.1	0°	0.303	0.84	36.16	−0.25%
0.71	–	0.241°	0.303	0.84	36.25	
0.71	0.1	1°	0.481	0.87	55.15	**2.17%**
0.71	–	1.276°	0.481	0.89	53.98	
0.71	0.1	2°	0.667	0.94	71.16	**4.56%**
0.71	–	2.318°	0.667	0.98	68.06	
0.71	0.1	3°	0.870	1.35	64.60	**14.96%**
0.71	–	3.374°	0.870	1.55	56.19	
0.725	0.1	−1°	0.129	0.83	15.49	−1.73%
0.725	–	−0.780°	0.129	0.82	15.76	
0.725	0.1	0°	0.312	0.82	37.17	**0.45%**
0.725	–	0.252°	0.312	0.84	37.00	
0.725	0.1	1°	0.500	0.88	56.92	**3.28%**
0.725	–	1.290°	0.500	0.91	55.11	
0.725	0.1	2°	0.700	1.06	66.26	**4.76%**
0.725	–	2.332°	0.700	1.11	63.25	
0.725	0.1	3°	0.896	1.98	45.29	**22.59%**
0.725	–	3.574°	0.896	2.43	36.94	

Table 2
Calculation of the power consumption and thrust generation to get a better estimation of the real drag savings for three example Mach numbers. The uncontrolled cases are shown in Table 1.

Ma	AoA	$c_{d,body} \cdot 10^2$	$c_{p,min}$	$c_{BLC} \cdot 10^2$	$c_{pump} \cdot 10^2$	$c_{D,total} \cdot 10^2$	Eff_{total}	
0.65	−1°	0.83	−0.49	−0.17	0.19	0.85	15.08	−6.35%
0.65	0°	0.84	−0.56	−0.17	0.20	0.87	35.85	−5.76%
0.65	1°	0.88	−0.67	−0.17	0.21	0.92	54.21	−5.28%
0.65	2°	0.91	−0.80	−0.17	0.23	0.97	61.29	−4.78%
0.65	3°	0.98	−0.94	−0.17	0.24	1.06	71.08	−1.86%
0.71	−1°	0.83	−0.56	−0.15	0.18	0.86	14.80	−5.42%
0.71	0°	0.84	−0.65	−0.15	0.19	0.88	34.60	−4.56%
0.71	1°	0.87	−0.80	−0.15	0.21	0.93	51.93	−3.80%
0.71	2°	0.94	−1.03	−0.15	0.23	1.02	65.64	−3.57%
0.71	3°	1.35	−1.32	−0.15	0.26	1.46	59.70	**6.24%**
0.725	−1°	0.83	−0.59	−0.15	0.18	0.86	14.94	−5.19%
0.725	0°	0.84	−0.69	−0.15	0.19	0.88	35.43	−4.25%
0.725	1°	0.88	−0.87	−0.15	0.21	0.94	53.26	−3.36%
0.725	2°	1.06	−1.16	−0.15	0.24	1.15	60.99	−3.56%
0.725	3°	1.98	−1.41	−0.15	0.27	2.10	42.75	**15.72%**

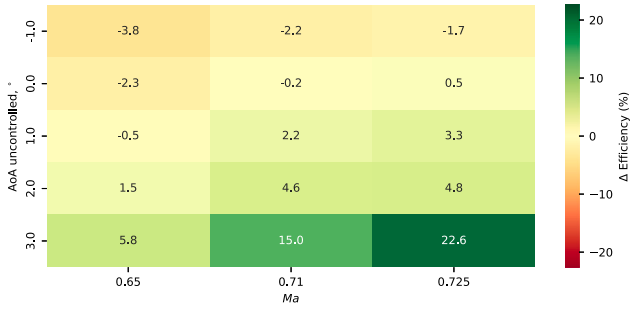

Fig. 12. Efficiency increase for suction on the suction side at three different Mach numbers of $Ma = 0.65$ as a representation of the subsonic case and $Ma = 0.71$ and 0.725 as representations for the transonic cases without the power consumption.

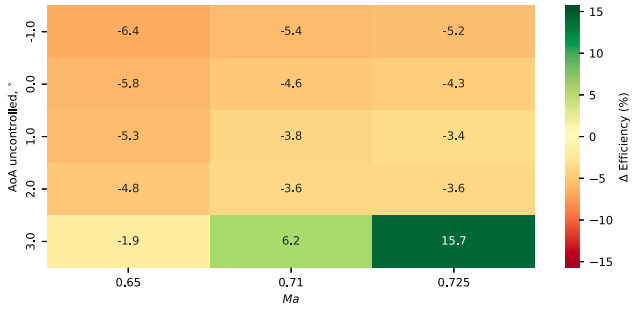

Fig. 13. Efficiency increase for suction on the suction side at three different Mach numbers of $Ma = 0.65$ as a representation of the subsonic case and $Ma = 0.71$ and 0.725 as representations for the transonic cases with the power consumption.

the efficiency of 4.76%.

A visualization of the efficiency increase for the different Mach numbers and angles of attack for the controlled cases is shown in Fig. 12. It can be seen that an increase in Mach number as well as an increase in the angle of attack (of the controlled case) leads to an increase in the efficiency.

As already discussed in Section 2.4 the active control method needs extra energy, which was not taken into account so far. To get an estimation if the control works and increases the efficiency, this extra power needs to be calculated. For all controlled cases, the minimal c_p value in the control area on the suction side was determined. Since all configurations in this chapter are of the control type suction, only the minimal c_p value needs to be taken into account. With the calculated pressure difference, the pump drag was determined by Eq. (5). The calculated values are shown in Table 2. The thrust that can be generated by dumping the fluid is calculated with the boundary layer penalty of Eq. (2). With the body drag, the generated thrust, and the pump drag, the total drag of the controlled cases was calculated. The newly calculated efficiency was then compared to the uncontrolled cases at the same c_l. Since the new total drag increased compared to the total drag without the energy consumption, the efficiency decreased. Now, most of the configurations show a decrease in efficiency. Also the case with the largest efficiency at $Ma = 0.725$ and $\alpha = 2°$ is now decreased by about −3.56%. An increase in efficiency can still be observed for configurations at high angles of attack. With a net efficiency of $Eff = 42.75$ in the 3° controlled case, an increase of 15.72% compared to the uncontrolled case was reached. This most promising configuration, achieved at a Mach number of 0.725, a control magnitude of $\dot{m}_{BLC} = 0.1\dot{m}_{\infty}$ and the control of suction on the suction side at $\alpha = 3°$, is shown in Fig. 14 and compared to the uncontrolled case at $\alpha = 3.574°$.

In Fig. 13 the change in efficiency of the controlled compared to the uncontrolled cases with low magnitude suction on the suction side is shown. As already observed before, an increase in Mach number and angle of attack (of the controlled cases) leads to higher values in ΔE, but by taking into account the calculation of the power consumption most of the cases now show an efficiency decrease. Only the high lift configurations in the transonic regime show an efficiency increase.

In the uncontrolled case, the pressure coefficient on the upper side before the shock is lower compared to the controlled case. As already seen in the previous results, suction on the suction side shifts the shock towards the trailing edge even though now two configurations with the same c_l are compared instead of the same AoA. In the plot of the friction coefficient, a flow separation on the suction side in the uncontrolled case can be observed right after the shock took place. The flow reattaches, and the friction coefficient recovers at about $x/c = 0.6$. In the controlled suction case, an increased friction coefficient in the controlled area can be observed. Although the friction coefficient is significantly higher than in the uncontrolled case, the shift of the shock position towards the trailing edge and the increase in magnitude still lead to a flow separation right after the shock takes place. The recovery of the friction coefficient is much faster than in the uncontrolled case, and only a very small separation bubble can be observed, but a flow separation cannot be prevented by the active flow control.

As already mentioned in Section 2.4 the estimation of the power consumption is very conservative and probably lower in a real-life scenario, as the pressure difference between the supply chamber and the airfoil's surface is very large in the region after the shock. Nevertheless, there are a few configurations where even with the conservative

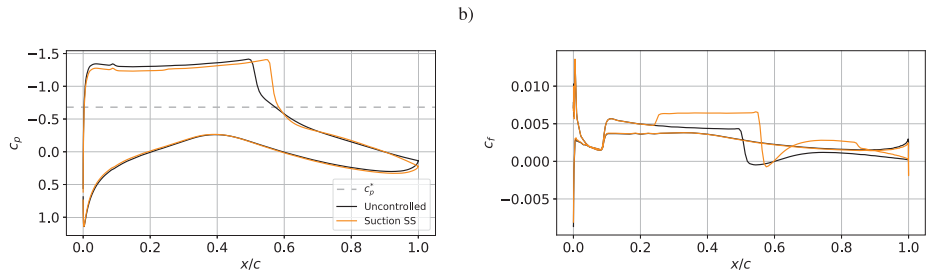

Fig. 14. Pressure and friction coefficient of the most promising configuration for $Ma = 0.725$, $m_{BLC} = 0.1$ and $\alpha = 3°$ or $3.567°$ for the controlled (suction on the suction side) and uncontrolled case, respectively.

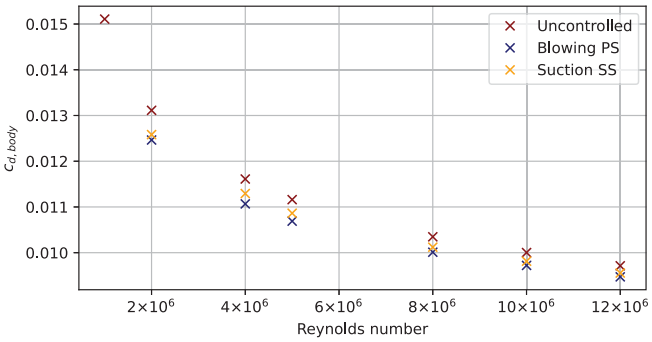

Fig. 15. Variation of the Reynolds number for one single configuration at a Mach number of $Ma = 0.725$ and a constant lift coefficient of $c_l = 0.695$.

power calculation a net drag saving could be achieved. Additionally, no optimization of different configurations was conducted so far, and some non-optimal cases were investigated as well to get an idea of the potential of the investigated control method.

3.3. Effect of Reynolds number

The parametric study was performed at a constant Reynolds number of $Re = 5 \times 10^6$ since the computational costs for a variation of the Reynolds number for the whole parametric study would have been too high. To see the effect of this variation, Reynolds numbers between $Re = 2 \times 10^6 - 12 \times 10^6$ are tested for the case of a Mach number of $Ma = 0.725$ and at a constant lift coefficient of $c_l = 0.695$ (which corresponds to the uncontrolled case at a Reynolds number of $Re = 5 \times 10^6$ and an angle of attack of $\alpha = 2.31°$). Fig. 15 shows the body drag as a function of the Reynolds number for the uncontrolled case as well as for the controlled cases of suction on the suction side and blowing on the pressure side. Overall the body drag is decreasing for all investigated configurations, but the rate of the decrease decreases with increasing Reynolds number. Also, the difference between the uncontrolled body drag and the controlled body drag decreases. Thus, the effects on the efficiencies are also decreasing. While at a Reynolds number of $Re = 5 \times 10^6$ for the investigated case, an efficiency increase of 2.7% is observed, at a Reynolds number of $Re = 10 \times 10^6$ the efficiency increase is 1.9%. The efficiency is calculated with the body drag, thus the costs for the control are not taken into account for this discussion.

In order to make a precise and detailed prediction about the influence of the Reynolds number, a more broadly diversified parametric study would have to be carried out. In the investigated set of mesh generation, code, and parameters used here, a wider range of Reynolds numbers cannot be covered. A more detailed discussion of the realization of the presented flow control method can be found in the Concluding discussions.

4. Concluding discussion

In the present study, the active control method of wall-normal uniform blowing and suction within a turbulent boundary layer has been assessed as a possible mean to achieve an increase in the aerodynamic efficiency of a transonic airfoil. RANS simulations with a fixed transition at 10% of the chord length to ensure a fully turbulent boundary layer are conducted. The flow regimes span from the subsonic regime to the transonic regime. The performance of the active control in the compressible but still subsonic regime as well as the presence of non-linear effects as the shock in the transonic regime are addressed in the present study.

The parametric study includes angles of attack of $\alpha = -1°$ to $3°$, the Mach number range covers $Ma = 0.600 - 0.729$, and a fixed Reynolds number of $Re = 5{\times}10^6$ is chosen. The control intensity is varied between $\dot{m}_{BLC} = (0.1 - 3)\dot{m}_\infty$ and four control positions are investigated, where the largest spans from 25%–85% of the chord length, and the three smaller ones are defined with respect to the shock position and span 10% of the chord length. Three different control configurations with uniform mass flow rates are investigated. With the inclusive drag, the efficiency was calculated and compared to the uncontrolled cases to make statements about whether the control leads to positive effects. The power consumption is estimated to also take into account the additional energy that is needed to run the active control.

The investigated blowing configurations of blowing on the suction side and blowing on the pressure side led to an increase in the inclusive drag compared to the uncontrolled cases. The most promising configuration that was found in the investigated setup is suction on the suction side.

In the subsonic regime, suction was mainly promising for high lift coefficients and low control magnitudes. In the transonic regime, most of the configurations with a low control magnitude showed a decreased inclusive drag and thus an increase in the efficiency. The suction configuration leads to a decrease in the pressure drag, but an increase in the friction drag. Opposite effects are observed for the blowing configurations. The results in the subsonic regime agree with previous investigations (Fahland et al., 2021, 2024; Atzori et al., 2020), who figured out that most configurations do not lead to an efficiency increase. In the transonic regime, the non-linear effect of the shock appears. The control leads to a shift of the shock position as well as a change in the shock magnitude. For suction on the suction side, the shock is shifted towards the trailing edge and increases in size; this leads to a decrease in the inclusive drag and an increase in efficiency. Many previous investigations showed that blowing leads to a reduction of the friction coefficient, which was also observed in the present parametric study. However, when the inclusive drag is calculated and also the pressure drag is taken into account, the method of blowing does not show a positive effect on the efficiency. With the inclusive drag, only the control of suction on the suction side shows a positive effect on the efficiency.

When the control magnitude is increased for suction on the suction side, the observed effects of the shift of the shock position towards the

trailing edge and the growth in magnitude increase as well. Only for low control magnitudes of $\dot{m} = 0.1 - 0.2\dot{m}_\infty$ a positive effect on the efficiency could be observed. Suction leads to an increase in the friction drag since the boundary layer thickness is decreased. This increase is growing with increasing control magnitude. The shift of the shock position has two effects: slight growth of the pressure drag, which also increases with increasing control magnitude, and an increase in the lift coefficient when comparing results at the same angle of attack. The combination of an increasing drag and lift results in an increase in efficiency for low magnitude control configurations. For the configurations with higher control magnitudes, the increase of the drag due to the increase in both drag components leads to an efficiency decrease.

The effect of smaller control positions, which are chosen with respect to the shock position, is much smaller than the larger control position, which can be explained by the smaller mass flow. Nevertheless, it is interesting to notice that not the exact position of the control seems to be important for its effect, but rather the configuration (blowing or suction) and the control magnitude.

Overall, when not taking into account the power consumption, low magnitude control configurations with suction on the suction side in the large control area at high lift coefficients lead to an increase in efficiency of up to 22% for the transonic case. The effect increases with increasing Mach number (appearance of the non-linear effect of the shock) and increasing angle of attack (closer to the design point of the airfoil). Since an active control is applied the additional energy which needs to be provided to run the control needs to be taken into account. A precise estimation of the energy required involves many assumptions and therefore leads to imprecise and no longer transparent results, a simpler and therefore more conservative estimation was chosen in this case. Even with the conservative estimation of the power consumption, some cases still show an efficiency increase. The high lift configurations show a decrease in the inclusive drag and thus an increase in efficiency of up to 16%. As discussed above, the estimation of the power consumption is conservative. A lower power consumption could be reached for example, by having two supply chambers, one at the actual pressure level before the shock and a second that sucks in the fluid in the rear part of the control region, where a lower pressure value would be sufficient. In the back part of the airfoil, the pressure difference between the supply chamber and the control surface is very high with the assumptions made for the power calculations present in the study. This would be one option to be more efficient, especially at lower angles of attack, which correspond to the cases with the highest absolute value of efficiency.

The results of the present study on wall-normal homogeneous blowing and suction show that the control of blowing does not lead to an increase in efficiency in any of the cases investigated. Positive results were achieved in a few cases of the control with suction, where a significant increase in efficiency is determined, but these cases neither correspond to the design points of the airfoil nor are present in a typical mission of a cruise aircraft. In the optimal operation points, for which the absolute efficiency is the highest, no increase in efficiency is determined for this control either. In order to be able to evaluate the control conclusively and completely, the cruise condition cases need to be optimized to make a clear statement about the effectiveness at these points. Furthermore, a combination with laminar flow control (Beck et al., 2018) – not the focus of the present study – can be carried out to utilize the positive effects of suction.

CRediT authorship contribution statement

A. Frede: Methodology, Software, Investigation, Validation, Formal analysis, Visualization, Writing – original draft, Writing – review & editing. **D. Gatti:** Conceptualization, Writing – review & editing, Supervision, Project administration, Funding acquisition.

Declaration of competing interest

The authors declare the following financial interests/personal relationships which may be considered as potential competing interests: Annika Frede reports financial support was provided by Friedrich and Elisabeth Boysen-Foundation. If there are other authors, they declare that they have no known competing financial interests or personal relationships that could have appeared to influence the work reported in this paper.

Acknowledgments

Financial support by the Elisabeth and Friedrich Boysen-Foundation is greatly acknowledged.

The authors gratefully acknowledge the computing time made available to them on the highperformance computer HoreKa at the NHR Center Karlsruhe. This center is jointly supported by the Federal Ministry of Education and Research and the state governments, for HoreKa supercomputer the Ministry of Science, Research and the Arts Baden-Württemberg.

Appendix A. Validation

For the validation of the present RANS results, a direct numerical simulation (DNS) is performed with the code FLEW, developed by Soldati et al. (2024). FLEW is designed for performing DNS on structured grids defined on generalized curvilinear coordinates and is an extension of the cartesian code STREAmS (Pirozzoli, 2010). The numerical framework uses a hybrid discretization of the compressible Navier–Stokes equations, which combines the nearly-zero numerical dissipation of 8th-order central schemes, best suited to accurately describe turbulence structures, with the robustness of 7th-order Weighted Essentially Non-Oscillatory (WENO) schemes, required to capture shock waves.

The grid was generated with a modified version of the open-source software Construct2D (Prosser, 2013–2018), where a hyperbolic algorithm generates high-quality, smooth C-type meshes. The grid generated with the code for a Reynolds number of $Re = 3 \times 10^5$ consists of $4096 \times 512 \times 256$ nodes in streamwise (x), wall-normal (y), and spanwise (z) directions, respectively.

The C-mesh has a radius of $25c$ and the outflow of the domain is placed at $25c$ from the trailing edge of the airfoil with the chord length c. The flow is assumed to be periodic in spanwise direction with an extension of $0.1c$. Additionally to the freestream condition prescribed, non-reflective boundary conditions are imposed to prevent the shock wave from being reflected in the far field. On the airfoil, a no-slip adiabatic boundary condition is prescribed.

The validation of the RANS simulation is performed at a Reynolds number of $Re = 3 \times 10^5$, a Mach number of $Ma = 0.725$, and an angle of attack of $\alpha = 4°$. The distribution of the pressure and friction coefficient is shown in Fig. A.16. The forced transition of the flow at $x/c = 0.1$ was prescribed for the DNS simulation with a numerical tripping defined according to Schlatter and Örlü (2012), consisting of a weak random volume force acting in wall normal direction. Owing to the small value of the Reynolds number and the effect of the favorable pressure gradient present up to $x/c \approx 0.4$, it was observed that the boundary layer on the pressure side of the airfoil remains laminar despite the numerical tripping. At $x/c \approx 0.4$ the pressure gradient changes and is now positive, which leads to a separation of the flow on the lower surface with a consequent separation-induced transition and reattachment.

The semi-implicit scalar source employed to initiate the turbulent flow in the RANS simulations at large values of Re is not adequate to reproduce the complex scenario occurring at the low value of Re necessarily employed in the DNS. To capture the transition and separation correctly also in the RANS simulations, the Langtry-Menter transition

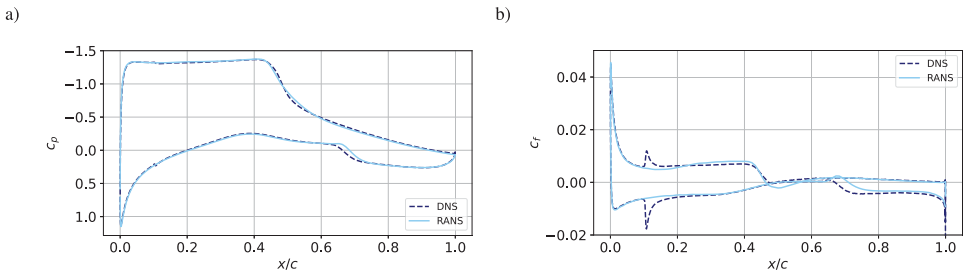

Fig. A.16. Distribution of the pressure and friction coefficient for a RANS and a DNS simulation at a Reynolds number of $Re = 3 \times 10^5$.

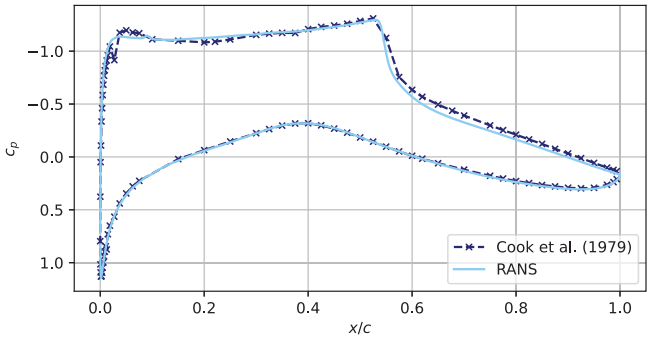

Fig. A.17. Pressure distribution of the RANS simulation and the experimental data of Cook et al. (1979) at a Reynolds number of $Re = 6.5 \times 10^6$.

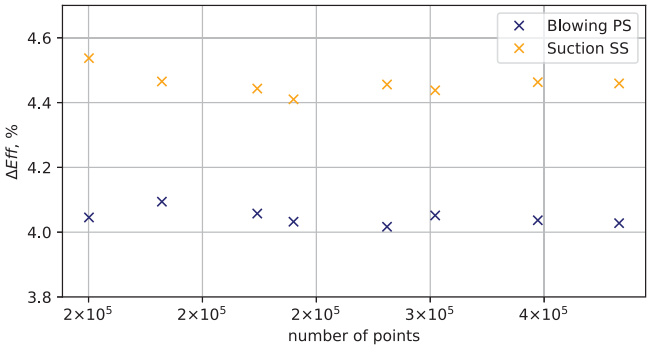

Fig. B.18. Change in efficiency of the controlled cases compared to the uncontrolled case for different mesh sizes.

Table A.3
Aerodynamic coefficients for the conducted validation simulation for the RANS and DNS results for a Reynolds number of $Re = 3 \times 10^5$.

	c_l	$c_{d,body} \cdot 10^2$	$c_{d,p} \cdot 10^2$	$c_{d,f} \cdot 10^2$
DNS	0.840	3.261	2.461	0.800
SU2	0.839	3.165	2.472	0.694

model has been utilized. The model predicts the transition and flow separation at the lower surface as expected and thus agrees with the DNS simulations. The LM transitional model was modified for the upper surface to trigger the transition at $x/c = 0.1$ on the upper surface.

The pressure distribution shows a good agreement between the DNS and the RANS simulations, see Fig. A.16. Both simulations capture the shock at the same position. Only the flow separation takes place slightly later on the airfoil's lower surface for the RANS simulation. This can also be observed in the distribution of the friction coefficient. Additionally, it can be seen that turbulence in the DNS simulation is triggered at $x/c = 0.1$.

In Table A.3 the aerodynamic coefficients for the validation simulations are shown. The lift coefficient agrees perfectly, while a small difference can be observed for the drag coefficient, which mainly comes from a difference in the friction drag. A small underestimation of the drag coefficient was also observed in the comparison of RANS and DNS by Fahland et al. (2021) for an incompressible flow. Despite the small deviation in the absolute value of the drag, the relative changes induced by the control were correctly reproduced in the RANS simulations.

While it is not possible to exploit DNS for validating the RANS simulations at the larger value of the Reynolds number of $Re = 5 \times 10^6$ employed in the present study, we can resort to laboratory experiments. So the pressure distribution of the RANS simulation at a Reynolds number of $Re = 6.2 \times 10^6$, a Mach number of $Ma = 0.734$, and an angle of attack of $\alpha = 2.79°$ (corrected for experimental wind tunnel blockage) is compared to the experimental data of Cook et al. (1979) (test case 9).

Fig. A.17 shows the pressure distribution of the RANS simulation and the experimental data of Cook et al. (1979). The data show a great agreement, where only the shock position is slightly shifted towards the trailing edge for the experimental data.

Finally, the validation of the RANS simulation with the DNS simulation at a Reynolds number of $Re = 3 \times 10^5$ and the comparison with the experimental data at a Reynolds number of $Re = 6.5 \times 10^6$ showed that the RANS simulations can resolve the flow and the most relevant flow physics.

Appendix B. Mesh convergence

The convergence of the mesh was tested with different meshes varying from 150 183 cells up to a very fine resolution of 382 915 cells. Fig. B.18 shows the increase in efficiency for blowing on the pressure side and suction on the suction side compared to the corresponding uncontrolled case. The simulations were conducted at a Reynolds number of $Re = 5 \times 10^6$, a Mach number of $Ma = 0.725$, an angle of attack of $\alpha = 2°$ and a control magnitude of $\dot{m}_{BLC} = 0.1\% \dot{m}_\infty$. For the calculation of the efficiency the body drag was used. Therefore, an increase in efficiency for cases with blowing is also achieved in these cases, since the drag component of the boundary layer penalty and the costs are not taken into account. For both control configurations, the deviations are minimal and are in the range $\Delta Eff = 0.15\%$. The simulations in the present study were carried out with the coarsest grid tested, as this already depicts all characteristics.

Data availability

Data will be made available on request.

References

Atzori, M., Vinuesa, R., Fahland, G., Stroh, A., Gatti, D., Frohnapfel, B., Schlatter, P., 2020. Aerodynamic effects of uniform blowing and suction on a NACA4412 airfoil. Flow Turbul. Combust. 105 (3), 735–759. http://dx.doi.org/10.1007/s10494-020-00135-z.

Beck, N., Landa, T., Seitz, A., Boermans, L., Liu, Y., Radespiel, R., 2018. Drag reduction by laminar flow control. Energies 11 (1), 252. http://dx.doi.org/10.3390/en11010252.

Black, T., Sarnecki, A., Mair, W., 1958. The Turbulent Boundary Layer with Suction or Injection. Vol. 20, ARC Cambridge, UK, Cambridge, UK.

Choi, J.-I., Xu, C.-X., Sung, H.J., 2002. Drag reduction by spanwise wall oscillation in wall-bounded turbulent flows. AIAA J. 40 (5), 842–850. http://dx.doi.org/10.2514/2.1750.

Cook, P.H., McDonald, M.A., Firmin, M.P., 1979. Aerofoil RAE2822 - Pressure Distributuions, Boundary Layer and Wake Measurements. AGARD Report AR.

Economon, T., Palacios, F., Copeland, S., Lukaczyk, T., Alonso, J., 2015. SU2: An open-source suite for multiphysics simulation and design. AIAA J. 54 (3), 828–846. http://dx.doi.org/10.2514/1.J053813.

Fahland, G., Atzori, M., Frede, A., Stroh, A., Frohnapfel, B., Gatti, D., 2024. Drag assessment for boundary layer control schemes with mass injection. Flow Turbul. Combust. http://dx.doi.org/10.1007/s10494-023-00462-x.

Fahland, G., Stroh, A., Frohnapfel, B., Atzori, M., Vinuesa, R., Schlatter, P., Gatti, D., 2021. Investigation of blowing and suction for turbulent flow control on airfoils. AIAA J. 59 (11), 4422–4436. http://dx.doi.org/10.2514/1.J060211.

Ferziger, J.H., Perić, M., 2002. Computational Methods for Fluid Dynamics, third ed. Springer, http://dx.doi.org/10.1007/978-3-642-56026-2.

Graver, B., Zhang, K., Rutherford, D., 2019. Emissions from commercial aviation, 2018. In: International Council on Clean Transportation.

Gad-el Hak, M., 2000. Flow Control: Passive, Active, and Reactive Flow Management. Cambridge University Press, http://dx.doi.org/10.1017/CBO9780511529535.

Huang, L., Huang, P.G., LeBeau, R.P., Hauser, T., 2004. Numerical study of blowing and suction control mechanism on NACA0012 airfoil. J. Aircr. 41 (5), 1005–1013. http://dx.doi.org/10.2514/1.2255.

Hwang, D., 2004. Review of research into the concept of the microblowing technique for turbulent skin friction reduction. Prog. Aerosp. Sci. 40 (8), 559–575. http://dx.doi.org/10.1016/j.paerosci.2005.01.002.

Kametani, Y., Fukagata, K., 2011. Direct numerical simulation of spatially developing turbulent boundary layers with uniform blowing or suction. J. Fluid Mech. 681, 154–172. http://dx.doi.org/10.1017/jfm.2011.219.

Mickley, H.S., Ross, R.C., Squyers, A.L., Stewart, W.E., 1954. Heat, mass, and momentum transfer for flow over a flat plate with blowing or suction. Natl. Advis. Comm. Aeronaut. 3206.

Park, J., Choi, H., 1999. Effects of uniform blowing or suction from a spanwise slot on a turbulent boundary layer flow. Phys. Fluids 11 (10), 3095–3105. http://dx.doi.org/10.1063/1.870167.

Pirozzoli, S., 2010. Generalized conservative approximations of split convective derivative operators. J. Comput. Phys. 229 (19), 7180–7190. http://dx.doi.org/10.1016/j.jcp.2010.06.006.

Prandtl, L., Betz, A. (Eds.), 1932. Ergebnisse der aerodynamischen versuchsanstalt zu göttingen - IV. Lieferung. In: Göttinger Klassiker der Strömungmechanik, vol. 7, Göttingen University Press, Göttingen, http://dx.doi.org/10.17875/gup2009-104.

Prosser, D., 2013–2018. Construct2D. https://sourceforge.net/projects/construct2d/.

Quadrio, M., Ricco, P., Viotti, C., 2009. Streamwise-travelling waves of spanwise wall velocity for turbulent drag reduction. J. Fluid Mech. 627, 161–178. http://dx.doi.org/10.1017/S0022112009006077.

Roe, P., 1981. Approximate Riemann solvers, parameter vectors, and difference schemes. J. Comput. Phys. 43 (2), 357–372. http://dx.doi.org/10.1016/0021-9991(81)90128-5.

Schlatter, P., Örlü, R., 2012. Turbulent boundary layers at moderate Reynolds numbers: inflow length and tripping effects. J. Fluid Mech. 710, 5–34. http://dx.doi.org/10.1017/jfm.2012.324.

Schlichting, H., Gersten, K., 1997. Grenzschicht-Theorie, ninth ed., völlig neubearbeitete und erw. Aufl ed. Springer, Berlin ; New York.

Schrauf, G., 2005. Status and perspectives of laminar flow. Aeronaut. J. 109 (1102), 639–644. http://dx.doi.org/10.1017/S000192400000097X.

Soldati, G., Ceci, A., Pirozzoli, S., 2024. FLEW: A DNS solver for compressible flows in generalized curvilinear coordinates. Aerotec. Missili Spaz. 103, 413–425. http://dx.doi.org/10.1007/s42496-024-00199-4.

Spalart, P.R., McLean, J.D., 2011. Drag reduction: enticing turbulence, and then an industry. Philos. Trans. R. Soc. A 369 (1940), 1556–1569. http://dx.doi.org/10.1098/rsta.2010.0369.

Stroh, A., Hasegawa, Y., Schlatter, P., Frohnapfel, B., 2016. Global effect of local skin friction drag reduction in spatially developing turbulent boundary layer. J. Fluid Mech. 805, 303–321. http://dx.doi.org/10.1017/jfm.2016.545.

Sumitani, Y., Kasagi, N., 1995. Direct numerical simulation of turbulent transport with uniform wall injection and suction. AIAA J. 33 (7), 1220–1228. http://dx.doi.org/10.2514/3.12363.

Szodruch, J., 1991. Viscous drag reduction on transport aircraf. AIAA Pap..

Walsh, M.J., 1986. Riblets for aircraft skin-friction reduction. In: Langley Symposium on Aerodynamics, Volume 1.

Walsh, M.J., Sellers, III, W.L., Mcginley, C.B., 1989. Riblet drag at flight conditions. J. Aircr. 26 (6), 570–575.

Yakeno, A., Hasegawa, Y., Kasagi, N., 2014. Modification of quasi-streamwise vortical structure in a drag-reduced turbulent channel flow with spanwise wall oscillation. Phys. Fluids 26 (8), 085109. http://dx.doi.org/10.1063/1.4893903.